Homothetic Design in Synchronous Reluctance Machines and Effects on Torque Ripple

Mukhammed Murataliyev, *Student Member, IEEE,* Michele Degano, *Member, IEEE*, Mauro Di Nardo, *Member, IEEE*, Nicola Bianchi, *Senior Member, IEEE,* Alberto Tessarolo, *Senior Member, IEEE*, Werner Jara, *Member IEEE*, Michael Galea*, Senior Member, IEEE,* Chris Gerada, *Senior Member, IEEE*.

Abstract—This paper presents a novel design concept for Synchronous Reluctance (SynRel) machines aimed at reducing the torque ripple. Two general sizing approaches based on the homothetic scaling principle are defined and compared. An in depth analysis on the torque ripple, for a wide range of scaled geometries, evaluated by finite element, has been carried out at different operating conditions. A further analysis is performed on 4 scaled geometries that have been optimized starting from 4 random rotor geometries. It is shown that the main rotor geometrical variables converge to similar values for all scaled machines. The accuracy of the proposed model is then validated by comparing the FE simulated torque ripple waveforms with the experimental data carried out, for a range of operating conditions, on a machine prototype. The outcome of this work is a fast and accurate scaling technique for the preliminary design of SynRel machines with reduced torque ripple.

Index Terms— Synchronous Reluctance Machines, Analytical modelling, Saliency ratio, Sizing Methods, Torque Ripple Optimization.

I. INTRODUCTION

Synchronous reluctance (SynRel) machines and their associated permanent magnet assisted variants are rapidly gaining market shares over the traditional electrical machine topologies in a wide range of applications. This increased interest results from the reduced use of rare earth materials, improved efficiency and field weakening capability. Despite these advantages, the main pitfall of this machine topology is the conspicuous torque oscillation, which is an undesired torque component causing acoustic noise, vibration and may degrade the drive controllability. Several techniques for the torque ripple reduction have been investigated over the last two decades and they can be classified into two major categories. The first one acts on the control scheme [1], [2], [3], while the second consists of specifically tailored motor-design techniques [4], [5]. The first approach is more broadly applicable, but it complicates the control algorithm structure and so its computational cost. While, the second approach obviously requires the development of new machine designs and this is not always possible. Several design techniques have been proved effective in minimizing torque oscillations, such as

suitable choice of the flux barriers with respect to the number of stator slots [6], suitable flux barrier angular displacement [7], [8], rotor skewing [9], etc. The proposed design guidelines originate from considerations based on analytical models, which often rely on a set of hypotheses introduced to simplify the analysis, and to make it feasible. Such analytical models most of the time neglect the effect of the non-linearities and geometrical complexities on the predicted performance. Therefore, they are useful only during the preliminary design stage. The next refining stage is then carried out by means of finite element (FE) analysis, which is able to evaluate the design aspects disregarded in the first stage (e.g. non-linearities heavily affect the torque profile). During the detailed design phase, several iterations are required and the computational cost depends also on the accuracy of the analytical model used in the preliminary design. Clearly, the more the analytical model is able to predict the machine performance faithfully, the less FE iterations are needed in the second design stage. Indeed, a more accurate analytical model is able to better identify the design space area to further explore via FE analysis. The second design stage is commonly implemented as a FE-based design optimization. Several works have addressed the problem of further reducing the computational burden required to carry out the optimization, which depends on two factors: the computational time required to evaluate the performance of a single machine candidate and the geometrical complexity of the machine structure to be optimized. The computation time varies according to which performance indexes are being optimized (torque, torque ripple, iron losses, etc.) and [4], [5], [10], [11] have been investigated the problem reaching a good trade-off between accuracy and computational burden. On the other hand, the geometrical complexity of the problem can be further reduced acting on how machine geometry under investigation is parametrized. In particular, [11] and [12] present a comparative study among different SynRel rotor flux barrier parametrizations, analysing the compromise between geometrical complexity and achieved performance. It is a general conclusion that adopting a flux barrier profile described by the Joukowski equation and a flux barrier parametrization

M. Murataliyev, M. Di Nardo, M. Degano, C. Gerada and M. Galea are with PEMC Group, University of Nottingham, Nottingham, UK.(email: mauro.dinardo4@nottingham.ac.uk, chris.gerada@nottingham.ac.uk)

N. Bianchi is with the Department of Electrical Engineering, University of Padova, Italy (email: nicola.bianchi@unipd.it)

A. Tessarolo with the Engineering and Architecture Department of the University of Trieste, Italy (email: atessarolo@units.it)

W. Jara is with the School of Electrical Engineering, Pontificia Universidad Catolica de Valparaíso, Valparaíso, Chile. (email: werner.jara@pucv.cl)

described by three parameters (barrier thickness, air gap angle and end-barrier parameter) is the best compromise between performance and geometrical complexity [12], [13]. These parameters are also the ones which most affect the torque performance, and for this reason they usually optimized during the FE refinement.

The purpose of this paper is to show how the FE design stage can be greatly simplified and so computationally relieved by considering a novel dimensioning homothetic approach during the first analytical design step. The homothetic scaling design principle was initially introduced for the induction motors in [14], and for permanent magnet synchronous motors in [15]. In this paper this concept is proposed for SynRel machines based on the analytical model presented in [16]. This work, which is a continuation of the authors' previous research on homothetic scaling for the design of synchronous reluctance machines [17], addresses the effect of different scaling approaches on the torque ripple.

The paper is structured as follows. In Section II the reference machine geometry is defined along with the homothetic design scaling principle. Then two scaling methods are assessed in Section III and different geometries are evaluated over a wide range of operating conditions, by means of FE simulations. In Section IV, four scaled machines are optimized minimizing their torque ripple and to show the correlation between the initial scaled geometry and the optimized one. The design approach is then validated in section V, comparing the torque ripple of the scaled machines, computed by means of FE simulations, against the experimental measurements on the reference machine prototype for different operating conditions.

II. Scaling Principle and Reference Machine Design

In the following two subsections, the preliminary sizing method of the reference machine is outlined along with the scaling principle. The sizing approach has been extensively described in [16], where the anisotropy of the rotor is considered as an input of the design procedure.

A. Preliminary sizing of the reference machine

The general sizing approach for a SynRel machine starts from the well-known torque equation written in the classical synchronous $(d\text{-}q)$ reference frame:

$$T_{em} = 1.5p(L_d - L_q)i_d i_q \sim$$
$$\sim 1.5p(K_{dm}L_m - K_{qm}L_m)i_d i_q \qquad (1)$$

where L_d and L_q are direct and quadrature inductances and i_d, i_q are direct and quadrature currents, whereas p is the number of poles. K_{dm}, K_{qm} are $d\text{-}q$ axes magnetizing coefficients, which are related to the salient nature of the reluctance machines and can be derived as:

$$K_{dm} = \frac{B_{1d}}{B_1} = \frac{L_{dm}}{L_m} \qquad (2)$$

$$K_{qm} = \frac{B_{1q}}{B_1} = \frac{L_{qm}}{L_m} \qquad (3)$$

As presented in equations (2) - (3), B_1 represents the fundamental component of the air-gap flux density for a uniform air-gap machine (no saliency) and B_{1d}, B_{1q} are set to be the fundamental flux-density components along the d and q

axes under produced by the same stator ampere-turns. Hence, ratios of fundamental flux density components are defined as magnetizing coefficients. Using equations (1) – (3) the saliency ratio can be derived as proposed in [16]:

$$\xi = \frac{L_d}{L_q} = \frac{L_m K_{dm} + L_l}{L_m K_{qm} + L_l} \sim \frac{L_m K_{dm} + L_m K_{qm}}{2 L_m K_{qm}} \qquad (4)$$

where L_l represents the leakage inductance. Based on equations (2) – (4) the saliency ratio ξ and magnetizing coefficients can be analysed using permeance functions along d and q axes described in [16].

For a 3-phase distributed winding cylindrical machine, the magnetizing inductance L_m is calculated as shown in (5), where R_{ro} is the rotor diameter, L_{stk} is the stack length, q is the number of slots per pole per phase, g is the air gap length, μ_0 is the relative permeability of air. K_{w1} and K_s are winding factor for the fundamental component and saturation coefficient, respectively, and n_s – is the number of turns per phase [18]:

$$L_m = 3\mu_0 D_{ro} L_{stk} \frac{(q K_{w1} n_s)^2}{g(1 + K_s)} \qquad (5)$$

In (5) the parameters R_{ro} and L_{stk} are the variables of interest as these determine the size of the machine. In order to relate R_{ro} and L_{stk} the aspect ratio γ can be used (6):

$$\gamma = \frac{L_{stk}}{D_{ro}} \qquad (6)$$

The torque equation (1) can be further expanded using the equation (2) – (6) as it was shown in [16]:

$$D_{ro} = \sqrt{\frac{T_{em} \, \gamma \, \mu_0 q \, K_{dm}\sqrt{\xi}}{B_{1d}^2 \pi g \sqrt{1 + \left(\frac{1}{2\xi - 1}\right)^2 \xi}}} \qquad (7)$$

Fig. 1 reports the flow chart of the adopted sizing approach, which includes 5 steps. Starting from the performance requirements and the design constraints, the second step defines the initial guess values of the machine's saliency ratio ξ, the rotor's magnetic insulation ratio k_{air} [16] and the number of barriers k. Using all predefined parameters above, the machine is sized using equation (7) during the third step. The saliency ratio is then estimated with an analytical model based on the equations (2)-(4) [19] and then the electromagnetic torque is calculated with equation (1). The machines' torque can be tuned in an iterative fashion by either varying k, k_{air} or the main rotor diameter D_{ro}, depending on the performance specifications.
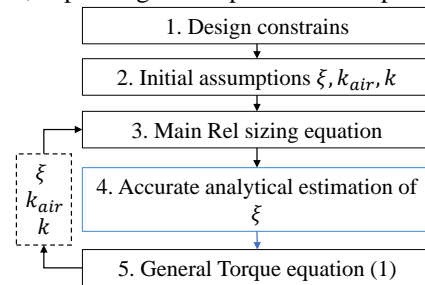
Fig. 1. The sizing principle algorithm.

The SynRel machine used in the following as reference design has been initially sized for a household appliance application whose design specification and constraints are listed in Table I. The winding layout was designed based on voltage-speed limit and the current density requirements [20]. Table I also reports the main dimensions and the winding details of the reference machine.

Table I. Design specifications, constrains and machine parameters

Symbol	Parameter	Quantity
J_{max}	Peak current density	4 A_{rms}/mm^2
k_{fill}	Slot fill factor	0.4
Q_s	Number of slots	24
$2p$	Pole numbers	4
m	Number phases	3
g	Air gap	0.3 mm
γ	Aspect ratio	0.84
k	Number of barriers	3
T_{em}	Rated Torque	0.9 Nm
n_b	Base speed	5000 rpm
I_{rms}	Phase Current	3.5A
V_{rms}	Phase Voltage	120V
D_{ro}	Rotor outer diameter	59 mm
L_{stk}	Stack length	48 mm
D_{so}	Stator outer diameter	100 mm
N_s	Number of turns per phase	128

B. Rotor design of the reference machine

The rotor geometry of the reference machine has been optimized to be suitable for both reluctance and permanent magnet assistant reluctance variants. For this reason, the rotor barriers are presenting a central rectangular slot, to host permanent magnets if needed, as shown in Fig. 2. The optimisation has been carried out considering the rotor parameters shown in Fig. 2 (i.e. barrier angles and thicknesses) and the optimization procedure is fully described in [21].
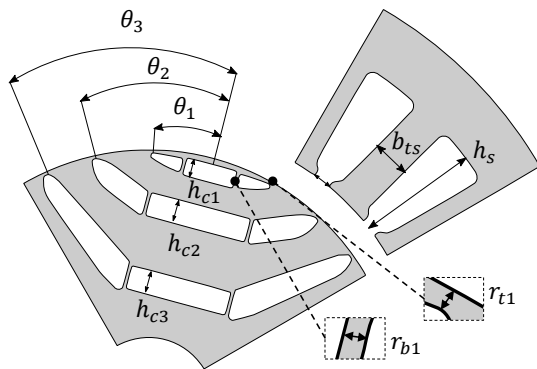
Fig. 2. Sketch of optimized benchmark machine M1.

C. Scaling principle

Based on the homothetic scaling principle discussed for Induction Machines in [14] as well as for the SynRel in [17] the reference machine can be scaled both radially and axially.

In the following, the aspect ratio of the scaled machines will be kept constant, therefore the stack length L_{stk} will be scaled proportionally to outer rotor diameter D_{ro}. The radial scaling can be carried out pursuing two approaches, i.e. keeping fixed the airgap length (AGF) and scaling the airgap length (AGS) with the same factor of the cross-sectional parameters. Equation (8) and (9) describe the scaling factors for the fixed airgap approach:

$$S_{si} = \frac{D_{si-n}}{D_{si-ref}} \qquad (8)$$

$$S_{ro} = \frac{D_{si-n} - 2g}{D_{si-ref} - 2g} \qquad (9)$$

where D_{si-n} is the stator inner diameter of the scaled machine, while D_{si-ref} is the stator inner diameter of the reference machine. Clearly, such approach utilizes two different scaling factors, S_{si} for the stator and S_{ro} for the rotor, while when scaling the airgap length as well, the scaling coefficients is the same for both stator and rotor (10):

$$S_{si} = S_{ro} = \frac{D_{si-n}}{D_{si-ref}} \qquad (10)$$

III. EVALUATION OF THE SCALED MACHINES TORQUE PERFORMANCE

In the following two subsections, the torque ripple of several scaled machines is FE evaluated for different operating points in the d-q axis current plane. In particular, in the first subsection two scaled machines are considered, one obtained keeping fixed the airgap length (M3) while the second (M2) also scaling the latter. Table II summarises the geometrical parameters featured by the scaled machines (M2 and M3) and the reference one (M1). In subsection III-B, the same analysis is extended to a wider range of scaling factors for both AGS and AGF cases, respectively.

Table II. Scaled geometries

Symbol	Parameter	Quantity M1	M2 (AGS)	M3 (AGF)
S_{si}	Stator scaling coefficient	1	1.5	1.5
S_{ro}	Rotor scaling coefficient	1	1.5	1.505
D_{si}	Stator inner diameter	59.6 mm	90 mm	90 mm
g	Air gap	0.3 mm	0.45 mm	0.3 mm
D_{ro}	Rotor outer diameter	59 mm	89.1 mm	89.4 mm
L_{stk}	Stack length	48 mm	75 mm	75.096 mm
D_{so}	Stator outer diameter	100 mm	153 mm	153 mm
D_{sh}	Shaft diameter	14 mm	22.5 mm	22.75 mm

A. FE evaluation of M1, M2 and M3 geometries

Fig. 3 presents the average and peak-to-peak torques of the three considered geometries in the *d-q* current plane. The first row of Fig. 3 (a and b) reports the torque performance of the reference geometry M1. The central row of Fig. 3 (c and d) shows the performance of the AGS geometry M2 while the bottom row (Fig. 3 e and f) represents the AGF geometry M3.

Fig. 3. Average torque and peak to peak torque on Id and Iq planes for M1, M2 and M3 machines.

It can be observed that the iso-curve of average torque does not vary significantly, which implies that the maximum torque per ampere (MTPA) locus is almost the same for the three machines as shown in Fig. 4 (y-axis represents the current excitation angle $\gamma^o=tan^{-1}(I_q/I_d)$). The latter reports the current phase angle corresponding to the MTPA condition as function of the current module for the reference and scaled machines. The average torque produced by the M2 geometry is lower compared to one obtained with the M3, i.e. at rated current density of 5A/mm^2 the average torque achieved by M2 $T_{M2}=$ 5.6Nm whereas $T_{M3}=$ 6.1Nm; this is clearly due to the bigger airgap of the M2 geometries respect to the M3 one.

Fig. 4. M1, M2 and M3 MTPA.

Fig. 5. Torque ripple vs peak phase current at MTPA.

Fig. 6. $T_\Delta(I_s, S_{si})$. Torque ripple vs Peak phase current at MTPA.

The torque ripple contours of the scaled geometries M2 and M3 follow the same pattern featured by the reference geometry (M1) as shown in Fig. 3b, d and f. Fig. 5 reports the percentage torque ripple of the three considered machines at the MTPA condition as function of the current amplitude. The torque ripple of the scaled M2 geometry follows almost the same pattern of the reference geometry M1 except for the really low and high current modules. This is due to bigger air gap; hence it requires higher current to properly saturate the ribs, as the machine was geometrically scaled. The scaled machine M3 shows a higher torque ripple respect to the reference geometry

M1 due to different scaling of rotor and stator. Based on all the above it can be concluded that both scaled machine, M2 and M3, feature a torque ripple comparable with the base geometry. In particular, the torque ripple variations lie within a 15% range over a wide range of currents. As can be observed at rated current density of 5A/mm^2, the M2 has $T_{\Delta M2}$~10.9% whereas M1 shows $T_{\Delta M1}$~11%; M3 shows relatively higher torque ripple $T_{\Delta M2}$~15%.

B. FE evaluation of wide range of scaled geometries

A total of 9 machines have been obtained within the range of $0.5 \leq S_{si} \leq 4$ by scaling the reference geometry M1 adopting both AGS and AGF approach. Fig. 6 a) and b) report the percentage torque ripple at MTPA condition in terms of contour in the plane stator inner radius - phase current.

Analysing the torque ripple of the machines uniformly scaled (AGS), it can be noticed that in for low current values (i.e. $5A \leq I_s \leq 20A$), the torque oscillation remains within the range $10\% \leq T_{\Delta} \leq 17\%$ for all the considered radial dimensions and current loading. On the contrary, the torque ripple shown in Fig. 6 b), related with the AGF geometries, show a significant increment compared to the reference machine M1.

A torque ripple within the range $10\% \leq T_{\Delta} \leq 17\%$ is obtained only for machine having $0.5 \leq S_{si} \leq 2$. It can be concluded that the AGS scaling approach leads to a moderate torque ripple variation over a wider range of scaling factor, whereas adopting the AGF scaling approach, the torque ripple variation is more pronounced.

IV. TORQUE RIPPLE OPTIMIZATION

The following exercise aims at demonstrating that starting from a random set of rotor parameters, the optimization algorithm converges to an optimal rotor with a geometry similar to the reference one. In order to demonstrate the above statement and the differences between AGS and AGF scaling approach, 4 different scaled machines have been considered and optimized.
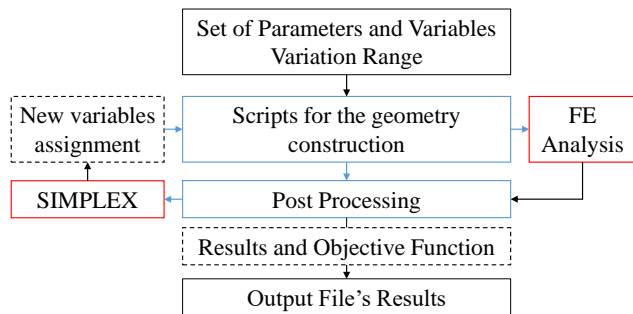
Fig. 7. Optimization workflow.

The first two (M2* and M3*) are the machines considered in Section III-A and whose parameters are detailed in Table II. The other two scaled machines (labelled as M4* and M5*) are obtained from the reference one adopting a scaling coefficient lower than one (S_{si}=0.75). The geometries M2* and M4* are obtained via the AGS approach while the M3* and M5* using the AGF method.

The geometrical variables to be optimized are the angles defining the barrier position at the airgap. Table III reports the lower and upper limits that those variables can assume during the optimization while the stator geometry remain fixed. The insulation ratio, defined as the per unit air portion of flux barriers along the q-axis:

$$k_{air} = \frac{2 \sum hc_k}{D_{ro} - D_{sh}} \qquad (11)$$

where D_{sh} is the shaft diameter and hc_k is the kth barrier thickness (as shown in Fig. 2), which is kept constant during the rotor optimization process.

Table III. Optimization input variables' boundaries

Parameter	Symbol	Boundaries		Unit
Flux barrier angle 1	θ_1	13	16	°
Flux barrier angle 2	θ_2	25	28	°
Flux barrier angle 3	θ_3	38	40	°
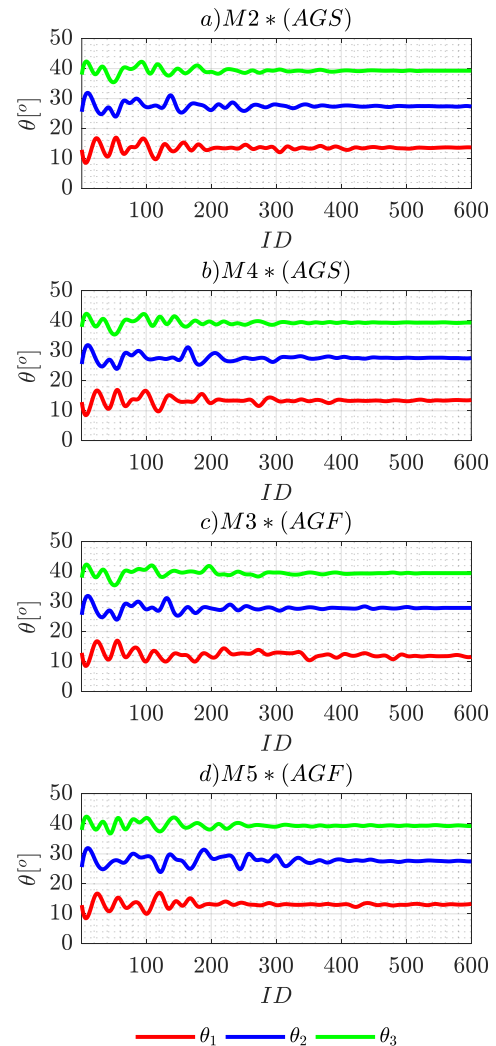
Fig. 8. Optimization variables trend of M2*, M3*, M4*, M5*.

The choice of keeping the insulation ratio (k_{air}) invariant during the optimization is related with the need of obtaining machine producing approximately the same average torque. Indeed, it has been demonstrated that the insulation ratio has a

	S_{si}=1.5		S_{si}=0.75	
	a) AGS	b) AGF	c) AGS	d) AGF
	424.4MPa	429.7MPa	105.5MPa	105.8MPa
	381.9MPa	386.8MPa	94.49MPa	95.23MPa
	339.5MPa	343.9MPa	84.41MPa	84.67MPa
	297.1MPa	300.1MPa	73.87MPa	74.1MPa
	254.7MPa	258.1MPa	63.32MPa	63.54MPa
	212.3MPa	215.1MPa	52.78MPa	52.98MPa
	169.9MPa	172.2MPa	42.24MPa	42.42MPa
	127.5MPa	129.3MPa	31.7MPa	31.86MPa
	85.0MPa	86.34MPa	21.16MPa	21.30MPa
	42.62MPa	43.41MPa	10.61MPa	10..74MPa
	0.204MPa	0.485MPa	0.074MPa	0.181MPa

Fig. 9. FE stress maps of scaled rotor geometries at n=18000 rpm

bigger impact on the average than the flux barrier angles as it has been shown in [22].

Table IV. Summary of the optimal flux barrier angles

	M1	M2*	M3*	M4*	M5*	Unit
θ_1	13.3	13.6	11.6	13.5	13.3	°
θ_2	27.6	27.3	27.9	27.6	27.5	°
θ_3	39.4	39.3	39.5	39.4	39.3	°

Table V. Details of validation

Label	S_{si}	Slot Area	I_s at J=4A/ mm²	I_s at J=5A/ mm²	A_s J=4A/ mm²	A_s J=4A/ mm²	Scaling principle
M1	1	68.2 mm²	4A	5A	16.57 kA/m	20.72 kA/m	-
M2	1.5	153.4 mm²	9A	11.25 A	10.97 kA/m	13.72 kA/m	AGS
M3	1.5	153.4 mm²	9A	11.25 A	10.8 kA/m	13.6 kA/m	AGF
M4	0.75	38.4 mm²	2.25 A	2.81 A	22.1 kA/m	27.62 kA/m	AGS
M5	0.75	38.4 mm²	2.25 A	2.81 A	22.2 kA/m	27.7 kA/m	AGF

With the choices motivated above, the optimisation problem presents a single objective function, the torque ripple. An heuristic optimiser (simplex algorithm) has been adopted to carry out the FE-based design optimization whose workflow is shown in Fig. 7. The initial Design of Experiments table used to start the search has been defined by a random sequence. The number of individuals for each generation has been set to 60 and a maximum of 10 generations has been considered leading to a total of 600 functional evaluations. An automatic drawing and solving procedure has been implemented via Matlab and the finite element software FEMM 4.2. The torque ripple (at MTPA condition with a current density of 5 A/mm^2) of each machine candidate is determined by a series of static simulation performed uniformly over one torque ripple period.

Fig. 8 shows how the geometrical variables converge to the optimal values leading to the minimum torque ripple for the scaled machines M2*, M3*, M4*, M5*. It can be clearly observed that the trends of the barrier angles converge approximately to the same angles. The summary of optimal angles is reported in Table IV. Based on the convergence of the angles value, it can be noticed that the variations of the θ_2 and θ_3 are not significant, all within a range of 0.4°, whereas the difference in θ_1 is significant only for M3* geometry. This can be explained by its disproportional scaling compared to other geometries, as it discussed in the previous section.

It can be concluded that the homothetic scaling, starting from a well-designed and optimized reference geometry, lead to a scaled design which is a solution that can be considered optimal, or for sure a good starting point for further torque ripple optimization refinements. Consequently, the design variable boundaries can be greatly restricted relieving the computational burden of the FE refinement design stage.

V.   MECHANICAL CONSIDERATIONS

In this section other mechanical aspects not previously considered are discussed. The thermal behaviour of the electrical machine is mainly a function of the current density, as well as the cooling type that is adopted by the system [21]. The current density was kept constant for all 5 machines including M1, therefore current was proportionally scaled, as the area of the slot is increased or decreased. As shown in Table V, the area of the slot is scaled by S_{si}^2. Electric loading A_s is highlighted in Table V to illustrate the difference among the analysed motor variants.

In a SynRel motor, the design of both radial and tangential ribs has been investigated extensively [21], [23], [24]. The function of the iron ribs is to mechanically retain the rotor parts together and to withstand the centrifugal force depending on the speed of the machine. Hence the ribs thickness is mainly affected by the maximum speed and the rotor geometry. For example, if the scaling leads to thinner ribs the maximum allowable speed of the machine could be affected and a mechanical refinement is required to guarantee the structural

integrity of the rotor. In the presented homothetic method, the ribs have been scaled proportionally. This is valid within certain scaling range.

Table VI. Details of FE mechanical simulations

Symbol	Parameter	Quantity
$r_{b1}=r_{b2}=r_{b3}$	Radial ribs	0.7 mm
$r_{t1}=r_{t2}=r_{t3}$	Tangential ribs	0.6 mm
ρ_d	Density	7650 kg/m³
ε_p	Poisson's ratio	0.3
γ_{coef}	Young's coefficient	200 GPa
σ_{stress}	Yield Stress	440 MPa

Fig. 9 presents the FE simulated mechanical stress maps for 4 scaled geometries $S_{si} = 0.75, 1.5$ at n=18000rpm. Mechanical FE simulations were carried out considering the parameters of the original geometry M1 as shown in Table VI, with highlighted ribs thicknesses according to Fig. 2 and physical properties of the silicon steel used. As can be observed the smaller scaled geometries $S_{si} = 0.75$ have the peak stress at the ribs which is within the allowable value of the σ_{stress}, whereas the $S_{si} = 1.5$ scaled geometries are close to the yield stress σ_{stress}.

a) Max Stress [MPa]

b) Max Displacement [mm]

AGF   AGS
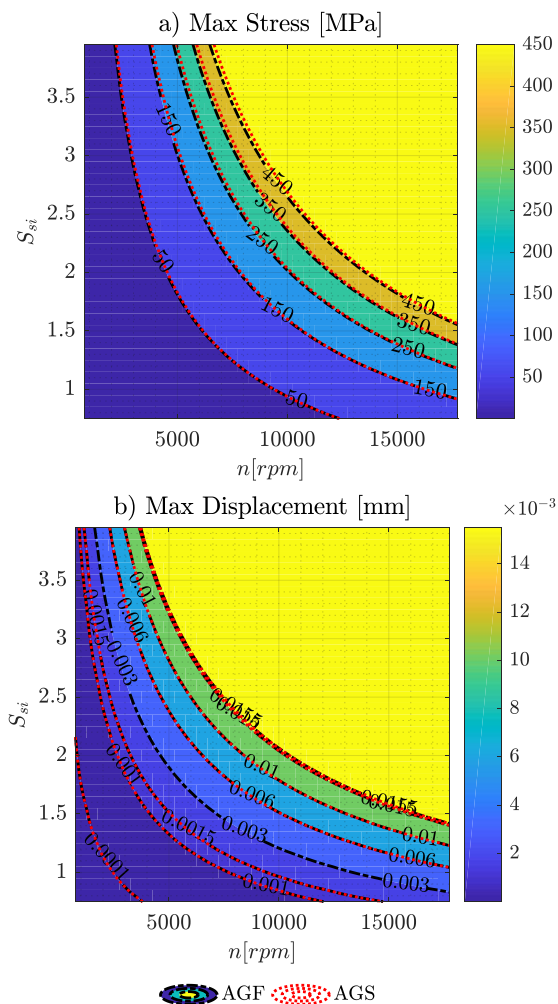
Fig. 10. Mechanical analysis of scaled geometries for AGS and AGF scaled geometries a) Maximum stress b) Maximum displacement c) Safety factor as functions of scaling factor S_{si} and rotational speed n in rpm

Fig. 10 presents the results for a wider speed range based on FE simulated mechanical stress test of 7 different geometries: 3 geometries were scaled based on (8) and (9) (AGF) and 3 geometries were scaled using (10) (AGS) and original geometry M1. Fig. 10 a) presents the maximum stress as function of scaling factor and speed where the maximum stress can be identified for different combination of the two parameters. The region depicted in yellow clearly shows mechanical unfeasible solutions which requires a further structural refinement stage. Fig. 10 b) presents the maximum displacement as function of scaling factor and speed.

Another mechanical consideration is related to the manufacturability of the rotor laminations. The thinnest part of the rotor lamination, i.e. the iron bridge, cannot be below a certain limit depending on the manufacturing method and selected material. In this case, it is not recommended to scale the original geometry M1 lower than S_{si}<0.75, as the ribs thickness will be lower than 0.45mm.

VI. CASE STUDY AND EXPERIMENTAL VALIDATION

In this section, four geometries are evaluated and compared to the prototype M1 (geometry presented in Table I). These were designed according to different scaling methods, two geometries using AGF (4) - (5) and two geometries using AGS (3), respectively. In the following subsections the evaluation of the torque ripple will be carried out for two current densities, 4 and 5 A/mm², respectively, using the data from Table V. The winding configuration, is kept constant, whereas the number of turns per phase N_s=128 for all machines.

A. FE torque ripple analysis for scaled machines

In Fig. 11 a) and b) the results of the torque ripple analysis, conducted for reduced-scaled machines M4 and M5 (S_s=0.75), considering different current angles and loading, are shown. In Fig. 11 a) the ripple oscillations, evaluated for a current angle of 45 electrical degrees (α^e=45º), are presented. At $J = 4\,A/mm^2$ their values are $T_{\Delta M4}$=15.1% and $T_{\Delta M5}$=13.23%, and at $J = 5\,A/mm^2$ are $T_{\Delta M4}$=11.72% and $T_{\Delta M5}$=10.79%, for M4 and M5, respectively. It can be observed that M4 achieves higher torque for both current profiles compared to M5, this is mainly due to the increased air gap with respect to rotor size, when the AGF scaling is applied.

According to the waveforms shown in Fig. 11 b), evaluated for a current angle of 50 electrical degrees (α^e=50º), the torque ripples at $J = 4\,A/mm^2$ are $T_{\Delta M5}$=13.18% and $T_{\Delta M4}$=12.7%, while at $J = 5\,A/mm^2$ are $T_{\Delta M5}$=11.78% and $T_{\Delta M4}$=10.1%, for M4 and M5, respectively.

The same analysis has been carried out in a similar fashion for the scaled machines M2 and M3 (S_s=1.5). The FE simulation results are shown in Fig. 11 c) and d). For a current density $J = 4\,A/mm^2$ their values are $T_{\Delta M3}$=15.71% and $T_{\Delta M2}$=11.15%, while at $J = 5\,A/mm^2$ are $T_{\Delta M3}$=16.7% and $T_{\Delta M2}$=11.69%, for M2 and M3, respectively. It can be observed that the torque ripple is increased for AGF scaled machine (M3), compared to AGS scaled (M2).

This confirms the behaviour shown in Fig. 4 and Fig. 6, where the machines that are scaled by AGF method have a
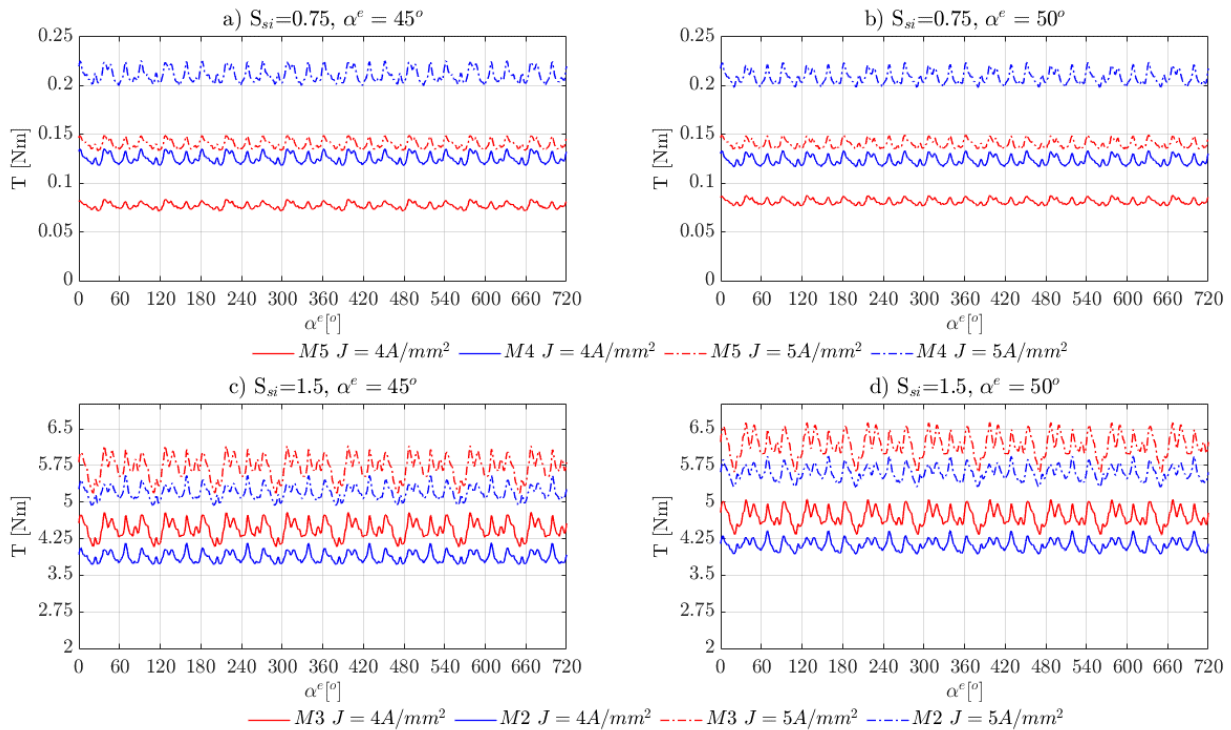
Fig. 11. FE evaluation of the torque ripple at different current angles (45 left, 50 right) and different current loading: a) and b) scaled machines $S_s = 0.75$, (M4 vs M5); c) and d) scaled machines $S_s = 1.5$, (M2 vs M3).

significant ripple increase for machines with larger diameter. On the contrary, the average torque of the M3 is higher with respect to M2. For the sake of clarity, a summary of the above results is reported in Table VII, that will be described in the following section.

B. Experimental results and validation

In order to validate the proposed theory, the SynRel machine M1, with 24 slots 4 poles, has been tested on an instrumented rig. The stator and rotor laminations of the prototype are shown in Fig. 12.

Fig. 12 M1 SynRel prototype front view.

The machine torque ripple has been characterised on a custom test rig presented in Fig. 13, described in detail in [26]. The tests are carried out at low speed in order to capture the high frequency nature of the torque oscillations. The motor M1 under test is connected through a torque meter to a master motor (dyno). Between the latter and the machine under test, a non-reversible gearbox is reducing the speed by a 1:59 ratio, as sketched in Fig. 13. The torque is measured for different current amplitudes and different current angles. The control algorithm is implemented on a dSpace 1104 platform.
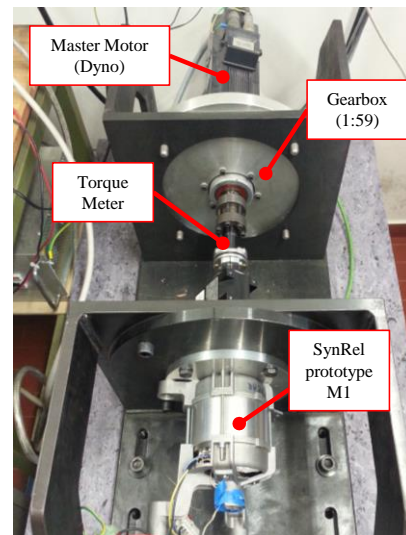
Fig. 13. Experimental test setup.

At first the test was carried out at current angle α^e=45°. Fig. 14 a) presents experimental and FE evaluation of the torque ripple waveforms at $J = 4$ A/mm² and $J = 5$ A/mm², at α^e=45°, respectively. As can be observed the torque ripple waveform determined via FE matches very well the experimental data. The measured torque ripple at $J = 4$ A/mm² is $T_{\Delta M1}$=13.4% with an average torque T=0.56Nm, whereas the FE evaluation gives $T_{\Delta M1}$=12.6% with average torque T=0.576Nm. For further validation, the same has been carried out for a higher current density value $J = 5$ A/mm², where the measured torque ripple is $T_{\Delta M1}$=11.21% with average torque T=0.89Nm, whereas the FE evaluation gives a value of $T_{\Delta M1}$=11.13% with an average torque T=0.89Nm.
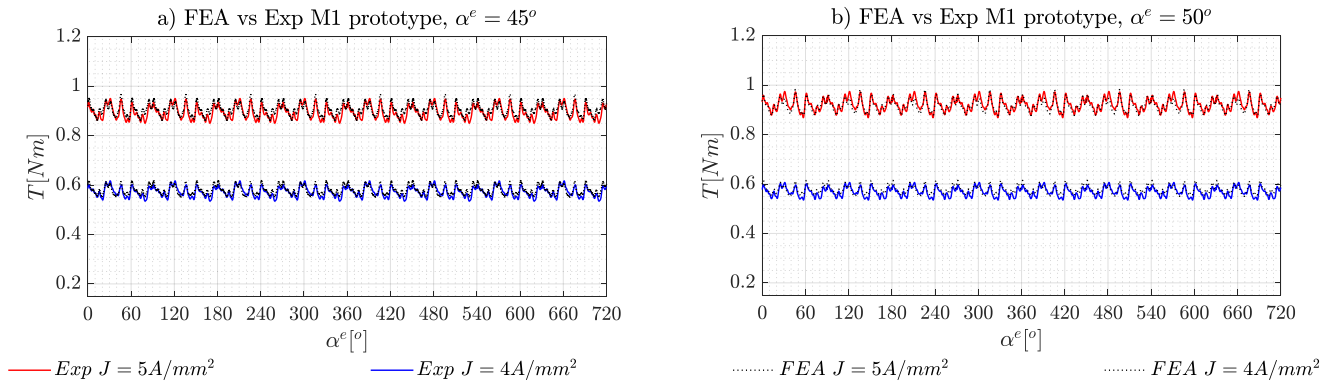
Fig. 14. Experimental and FE evaluation of the torque ripple on the reference machine M1: a) at 45 º current angle for different current loading; b) at 50 º current angle for different current loading.

Based on these results, it can be said that the FE simulations predict the torque ripple accurately, with a slight under estimation. In fact, the average error of about δ_{FEA}~2.4%. with respect to experimental data. Additional experimental tests have been carried out at a different current angle, α^e=50º. Fig. 14 b) shown the experimental and FE evaluation of the torque ripple waveforms at $J = 4\ A/mm^2$ and $J = 5\ A/mm^2$, at α^e=50º, respectively.

Table VII. Summary of the torque ripple evaluation

Label	T(Nm) at J=4A/mm²		T(Nm) at J=5A/mm²		T_Δ (%) at J=4A/mm²		T_Δ(%) J=5A/mm²	
α^e	45º	50º	45º	50º	45º	50º	45º	50º
M1 (EXP)	0.56	0.56	0.89	0.92	13.4	11.6	11.2	11.2
M1 (FE)	0.57	0.57	0.89	0.93	13.6	11.2	11.1	11.1
M2	3.87	4.12	5.2	5.6	11.2	11.5	11.7	11.1
M3	4.4	4.7	5.7	6.17	15.7	15.2	16.7	16.3
M4	0.12	0.12	0.21	0.21	15.1	12.7	11.7	12.7
M5	0.077	0.081	0.14	0.14	13.2	13.2	10.8	11.8

Similarly, to Fig. 14 a), these results are confirming again that the FE simulated torque ripple waveforms are in line with the measured data. The experimentally obtained torque ripples for a current angle α^e=50º, at $J = 4\ A/mm^2$, are $T_{\Delta M1}$=12.6% with average torque T=0.567Nm, whereas the FE ones $T_{\Delta M1}$=11.16% with average torque T=0.577Nm. For higher current density, $J = 5\ A/mm^2$, the experimental torque ripple is $T_{\Delta M1}$=11.21% with average torque T=0.921Nm, whereas FE $T_{\Delta M1}$=11.16% with average torque T=0.926Nm.

In order to summarise all the results from both experimental measurements and FE simulations, for the different operating conditions considered, Table VII is reporting the data for all machines analysed. Based on all the above it can be observed that the scaled machines present a torque ripple which is in close correlation with the reference machines, for both scaled and fixed air gap scaling principles.

This is a confirmation that the scaling method can be used, starting from a machine optimised for a minimum torque ripple, to re-design a larger or smaller machine with minimum effort.

VII.   CONCLUSION

This paper assesses the effect on the torque ripple of two homothetic scaling principles of synchronous reluctance machines. Two main scaling principles have been defined, which are the fixed air gap for the scaled machines AGF and scaled air gap for the scaled machines AGS. The correlations between the torque ripple of a reference machine with respect to a scaled machine is analysed in depth.

It has been demonstrated that the homothetic scaling method proposed leads to a design that can be considered optimal, or to a solution that is a good starting point for a further torque ripple optimization refinement. This approach is significantly reducing the computational time to obtain a machine with a minimum torque oscillation. In fact, all scaled machine has shown less than 5% increase in torque ripple with respect to reference machine. The torque ripple waveforms have been experimentally validated on manufactured prototype of the reference machine M1. The measured torque profiles are showing a very good match with respect to the FE evaluations. It can be concluded that the proposed method is defining a fast and accurate scaling technique for the preliminary design of the SynRel machines. This can be adopted by the industrial community, in particular when the performance assessment of a range of machine is required, starting from a reference design.

REFERENCES

[1] P. Mattavelli, L. Tubiana, and M. Zigliotto, "Torque-ripple reduction in PM synchronous motor drives using repetitive current control," *IEEE Trans. Power Electron.*, vol. 20, no. 6, pp. 1423–1431, 2005.

[2] N. Nakao and K. Akatsu, "Suppressing pulsating torques: Torque ripple control for synchronous motors," *IEEE Ind. Appl. Mag.*, vol. 20, no. 6, pp. 33–44, 2014.

[3] A. K. M. Arafat and S. Choi, "Active Current Harmonic Suppression for Torque Ripple Minimization at Open-Phase Faults in a Five-Phase PMa-SynRM," *IEEE Trans. Ind. Electron.*, vol. 66, no. 2, pp. 922–931, 2019.

[4] M. Degano, M. Di Nardo, M. Galea, C. Gerada, and D. Gerada, "Global design optimization strategy of a synchronous reluctance machine for light electric vehicles," *IET*, 2016.

[5] N. Bianchi and H. Mahmoud, "An Analytical Approach to Design the PM in PMAREL Motors Robust Toward the Demagnetization," *IEEE Trans. Energy Convers.*, vol. 31, no. 2, pp. 800–809, 2016.

[6] S.-H. Han, T. M. Jahns, W. L. Soong, M. K. Güven, and M. S. Illindala, "Torque ripple reduction in interior permanent magnet synchronous machines using stators with odd number of slots per pole pair," *IEEE Trans. Energy Convers.*, vol. 25, no. 1, pp. 118–127, 2010.

[7] N. Bianchi, S. Bolognani, D. Bon, and M. D. Pré, "Rotor flux-barrier design for torque ripple reduction in synchronous reluctance and PM-assisted synchronous reluctance motors," *IEEE Trans. Ind. Appl.*, vol. 45, no. 3, pp. 921–928, 2009.

[8] M. Sanada, K. Hiramoto, S. Morimoto, and Y. Takeda, "Torque ripple improvement for synchronous reluctance motor using an asymmetric flux barrier arrangement," *IEEE Trans. Ind. Appl.*, vol. 40, no. 4, pp. 1076–1082, 2004.

[9] T. M. Jahns and W. L. Soong, "Pulsating Torque Minimization Techniques for Permanent Magnet AC Motor Drives-A Review," vol. 43, no. 2, 1996.

[10] H. Mahmoud, M. Degano, G. Bacco, N. Bianchi, and C. Gerada, "Synchronous Reluctance Motor Iron Losses: Analytical Model and Optimization," *2018 IEEE Energy Convers. Congr. Expo. ECCE 2018*, pp. 1640–1647, 2018.

[11] G. Pellegrino, F. Cupertino, and C. Gerada, "Automatic Design of Synchronous Reluctance Motors Focusing on Barrier Shape Optimization," *IEEE Trans. Ind. Appl.*, vol. 51, no. 2, pp. 1465–1474, 2015.

[12] M. Gamba, G. Pellegrino, and F. Cupertino, "Optimal number of rotor parameters for the automatic design of Synchronous Reluctance machines," *Proc. - 2014 Int. Conf. Electr. Mach. ICEM 2014*, pp. 1334–1340, 2014.

[13] R. R. Moghaddam and F. Gyllensten, "Novel high-performance SynRM design method: An easy approach for a complicated rotor topology," *IEEE Trans. Ind. Electron.*, vol. 61, no. 9, pp. 5058–5065, 2014.

[14] A. Tessarolo, M. De Martin, D. Diffen, M. Branz, and M. Bailoni, "Practical assessment of homothetic dimensioning criteria for induction motors," *7th IET Int. Conf. Power Electron. Mach. Drives, PEMD 2014*, pp. 1–6, 2014.

[15] S. Stipetic, D. Zarko, and M. Popescu, "Ultra-fast axial and radial scaling of synchronous permanent magnet machines," *IET Electr. Power Appl.*, vol. 10, no. 7, pp. 658–666, 2016.

[16] M. Murataliyev, M. Degano, and M. Galea, "A Novel Sizing Approach for Synchronous Reluctance Machines," *IEEE Trans. Ind. Electron.*, vol. 0046, no. 2, 2020.

[17] M. Murataliyev *et al.*, "A Homothetic Scaling Criteria for Synchronous Reluctance Machines Design," *IEEE Trans. Energy Convers.*, p. 1, 2020.

[18] P. Ponomarev, Y. Alexandrova, I. Petrov, P. Lindh, E. Lomonova, and J. Pyrhonen, "Inductance calculation of tooth-coil permanent-magnet synchronous machines," *IEEE Trans. Ind. Electron.*, vol. 61, no. 11, pp. 5966–5973, 2014.

[19] I. Boldea, Z. X. Fu, and S. A. Nasar, "Performance evaluation of axially-laminated anisotropic (ALA) rotor reluctance synchronous motors," in *Conference Record of the 1992 IEEE Industry Applications Society Annual Meeting*, pp. 212–218.

[20] J. Pyrhonen, T. Jokinen, V. Hrabovcova, and H. Niemela, *Design of Rotating Electrical Machines*. 2008.

[21] M. Degano, E. Carraro, and N. Bianchi, "Selection criteria and robust optimization of a traction PM-assisted synchronous reluctance motor," *IEEE Trans. Ind. Appl.*, vol. 51, no. 6, pp. 4383–4391, 2015.

[22] N. Bianchi, M. Degano, and E. Fornasiero, "Sensitivity analysis of torque ripple reduction of synchronous reluctance and interior PM motors," *IEEE Trans. Ind. Appl.*, vol. 51, no. 1, pp. 187–195, 2015.

[23] C. Babetto, G. Bacco, and N. Bianchi, "Synchronous Reluctance Machine Optimization for High Speed Applications," *IEEE Trans. Energy Convers.*, vol. 8969, no. c, pp. 1–8, 2018.

[24] M. Di Nardo, M Galea and C. Gerada, "Multi-physics Optimization Strategies for High Speed Synchronous Reluctance Machines," no. Im, pp. 2813–2820, 2015.

[25] M. Di Nardo, G. Lo Calzo, M. Galea, and C. Gerada, "Design optimization of a high-speed synchronous reluctance machine," *IEEE Trans. Ind. Appl.*, vol. 54, no. 1, pp. 233–243, 2017.

[26] N. Bianchi, E. Fornasiero, M. Ferrari, and M. Castiello, "Experimental comparison of PM-assisted synchronous reluctance motors," *IEEE Trans. Ind. Appl.*, vol. 52, no. 1, pp. 163–171, 2015.

Mukhammed Murataliyev received his M.Sc. degree in electrical engineering from the University of Nottingham, Semenyih, Malaysia in 2016. He is currently pursuing a Ph.D. degree at the University of Nottingham Ningbo China and UK, with a focus on novel synchronous reluctance motor design and optimization methods. His main research interest includes design and modeling of synchronous reluctance and permanent magnet machines for industrial and aerospace applications.

Michele Degano (M'15) received his Master's degree in Electrical Engineering from the University of Trieste, Italy, in 2011, and his Ph.D. degree in Industrial Engineering from the University of Padova, Italy, in 2015. Between 2014 and 2016, he was a post-doctoral researcher at The University of Nottingham, UK, where he joined the Power Electronics, Machines and Control (PEMC) Research Group. In 2016 he was appointed Assistant Professor in Advanced Electrical Machines, at The University of Nottingham, UK. He was promoted Associate Professor in 2020. His main research focuses on electrical machines and drives for industrial, automotive, railway and aerospace applications, ranging from small to large power. He is currently the PEMC Director of Industrial Liaison leading research projects for the development of hybrid electric aerospace platforms and electric transports.

Mauro Di Nardo received the M.Sc.(Hons.) degree in electrical engineering from the Polytechnic University of Bari (Italy) in 2012, and the Ph.D. degree in electrical machine design from the University of Nottingham (UK) in 2017. From 2017 to 2019 he was head of the AROL research team within the Polytechnic University of Bari leading industrial R&D projects on electrical drives design for mechatronics applications.
Since the 2019, he joined the Power Electronics and Machine Control Group of the University of Nottingham as Research Fellow.
His research interests are the analysis, modelling, and optimizations of electrical machines, including permanent magnet and synchronous reluctance topologies for automotive and aerospace sectors as well as induction motor for industrial applications.

Nicola Bianchi (Fellow, IEEE), received the M.Sc. and Ph.D. degrees in electrical engineering from the University of Padova, Padova, Italy, in 1991 and 1995, respectively. In 1998, he joined the Department of Electrical Engineering, University of Padova, as an Assistant Professor, where since 2005, he has been an Associate Professor in Electrical Machines, Converters, and Drives with the Electric Drive Laboratory, Department of Electrical Engineering. He has authored and coauthored several scientific papers and international books on electrical machines and drives. His research interests include the field of design of electrical machines, particularly for drive

applications. Dr. Bianchi was the recipient of five awards for best conference and journal papers. He is a member of the Electric Machines Committee and the Electrical Drives Committee of the IEEE Industry Applications Society. He was a Technical Program Chair for the IEEE Energy Conversion Congress and Exposition in 2014 and is currently an Associate Editor for the IEEE TRANSACTIONS ON INDUSTRY APPLICATIONS.

Alberto Tessarolo received his Laurea and Ph.D. degrees in Electrical Engineering from the University of Trieste, Italy, and Padova, Italy, in 2000 and 2011, respectively. Before joining the University, he worked in the design and development of large innovative motors, generators and drives. Since 2006, he has been with the Engineering and Architecture Department of the University of Trieste, Italy, where he teaches the courses of Electric Machine Fundamentals and Electric Machine Design. He leads several funded research projects in cooperation with industrial companies for the study and development of innovative electric motors, generators and drives. He has authored over 150 international papers in the area of electrical machines and drives. He has been an associated editor for IEEE TRANS. ON ENERGY CONVERSION, IEEE TRANS. ON INDUSTRY APPLICATIONS and IET ELECTRIC POWER APPLICATIONS, and presently serves as the Editor-in-Chief of the IEEE TRANS. ON ENERGY CONVERSION. Dr. Tessarolo is a member of the Rotating Machinery Technical Committee TC2 of the International Electrotechnical Commission (IEC) and supports the definition of IEC standards on inverter-fed electric motors. He is also a member of the IEEE Power and Energy Society Electric Machinery Committee, of the IEEE Industry Applications Society Electric Machines Committee and of the IEEE Industrial Electronics Society Electric Machines Technical Committee.

Werner Jara (S'15–M'17) received the B.Sc. degree in electrical engineering from the University of Concepción, Concepción, Chile, in 2010, and the D.Sc. degree from the University of Concepción, Concepción, Chile, and the Lappeenranta University of Technology, Lappeenranta, Finland, both in 2016. He is currently a Lecturer with the Department of Electrical Engineering, Pontificia Universidad Católica de Valparaíso, Valparaíso, Chile. His current research interests include the field of electrical machines and drives, particularly numerical modeling, and design of electromagnetic devices.

Michael Galea (M'13-SM'18, FRAeS) received his PhD in electrical machines design from the University of Nottingham, UK, where he has also worked as a Research Fellow. He is currently the Head of School of Aerospace in the University of Nottingham, Ningbo, China, where he is also the Director of Aerospace. He currently lectures in Electrical Drives and in Aerospace Systems Integration and manages a number of diverse projects and programmes related to the more / all electric aircraft, electrified propulsion and associated fields. His main research interests are design, analysis and thermal management of electrical machines and drives (classical and unconventional), the more electric aircraft and electrified and hybrid propulsion. He is a Fellow of the Royal Aeronautical Society and a Senior Member of the IEEE.

Chris Gerada (SM'12) is an Associate Pro-Vice-Chancellor for Industrial Strategy and Impact and Professor of Electrical Machines. His principal research interest lies in electromagnetic energy conversion in electrical machines and drives, focusing mainly on transport electrification. He has secured over £20M of funding through major industrial, European and UK grants and authored more than 350 referred publications. He received the Ph.D. degree in numerical modelling of electrical machines from The University of Nottingham, Nottingham, U.K., in 2005. He subsequently worked as a Researcher with The University of Nottingham on high-performance electrical drives and on the design and modelling of electromagnetic actuators for aerospace applications. In 2008, he was appointed as a Lecturer in electrical machines; in 2011, as an Associate Professor; and in 2013, as a Professor at The University of Nottingham. He was awarded a Research Chair from the Royal Academy of Engineering in 2013. Prof. Gerada served as an Associate Editor for the IEEE Transactions on Industry Applications and is the past Chair of the IEEE IES Electrical Machines Committee.